1   **KMT5C displays robust retention and liquid-like behavior in phase separated**

2   **heterochromatin**

3

4   Hilmar Strickfaden,[1] Kristal Missiaen,[1] Michael J. Hendzel,[1,2] and D. Alan Underhill[1,3,*]

5   Departments of [1]Oncology, [2]Cell Biology, and [3]Medical Genetics, Faculty of Medicine &

6   Dentistry, University of Alberta, Edmonton, Alberta, Canada

7

8   **Abstract**

9   The pericentromere exists as a distinct chromatin compartment that is thought to form by a

10   process of phase separation. This reflects the ability of the heterochromatin protein CBX5 (*aka*

11   HP1α) to form liquid condensates that encapsulate pericentromeres.[1,2] In general, phase

12   separation compartmentalizes specific activities within the cell, but unlike membrane-bound

13   organelles, their contents rapidly exchange with their surroundings.[3] Here, we describe a novel

14   state for the lysine methyltransferase KMT5C where it diffuses within condensates of

15   pericentromeric heterochromatin but undergoes strikingly limited nucleoplasmic exchange,

16   revealing a barrier to exit similar to that of biological membranes. This liquid-like behavior maps

17   to a discrete protein segment with a small number of conserved sequence features and containing

18   separable determinants for localization and retention that cooperate to confer strict spatial

19   control. Accordingly, loss of KMT5C retention led to aberrant spreading of its catalytic product

20   (H4K20me3) throughout the nucleus. We further found that KMT5C retention was reversible in

21   response to chromatin state, which differed markedly for CBX5 and the methyl-CpG binding

22   protein MeCP2, revealing considerable plasticity in the control of these phase separated

23   assemblies. Our results establish that KMT5C represents a precedent in the biological phase

1

24   separation[4] continuum that confers robust spatial constraint of a protein and its catalytic activity

25   without progression to a gel or solid.

26   Analyses of the prototypic heterochromatin protein CBX5 indicated that phase separation

27   plays an important role in partitioning of pericentromeric heterochromatin.[1,2] This is particularly

28   evident in mouse interphase nuclei where pericentromeres from multiple chromosomes form

29   chromocenters.[5] Despite the stable appearance of such assemblies, they are highly dynamic and

30   their protein constituents rapidly exchange with their surroundings, reflecting low affinity,

31   multivalent interactions that allow proteins to coalesce into distinct aqueous compartments.[6,7] In

32   this context, CBX5 enrichment within pericentromeric heterochromatin requires binding to

33   trimethyllysine-9 on histone H3 (H3K9me3), which is placed by the lysine methyltransferases

34   SUV39H1 and 2.[8] CBX5 then recruits KMT5C protein to catalyze histone H4 lysine-20

35   trimethylation (H4K20me3). In fluorescence recovery after photobleaching (FRAP), CBX5

36   rapidly exchanged between the pericentromere and nucleoplasm,[9] whereas SUV39H2 and

37   KMT5C appeared to be immobile when entire chromocenters were bleached.[10] Although

38   concluding that the latter two proteins created a stable scaffold,[10] these studies did not assess

39   mobility within chromocenters, which would instead suggest retention within a liquid

40   compartment. To test this fundamentally different model, we queried KMT5C dynamics within

41   mouse chromocenters in comparison to CBX5 and MeCP2, which also exhibits pericentromeric

42   enrichment and nucleoplasmic exchange.[10,11] As previously shown with full chromocenter

43   bleaching,[10,12] KMT5C displayed long recovery times, indicating minimal exchange with the

44   surrounding nucleoplasm, and was considerably slower than either CBX5 or MeCP2 (Fig. 1a,

45   Extended Data Videos 1-3). Upon partial bleaching, however, KMT5C fluorescence recovered

46   (Fig. 1a, Extended Data Videos 4 and 5) and progressed from the non-bleached portion of the

2

47   chromocenter (Fig. 1b). This occurred on a timescale where there was no appreciable recovery of

48   fully bleached chromocenters in the same nucleus (Fig. 1b), establishing that KMT5C moved

49   readily within chromocenters but did not efficiently exchange (Fig. 1c). In the context of phase

50   separation, this signifies a remarkable barrier to exit that has not been observed for other proteins

51   without transition to a solid or gel state, which renders them immobile.[13] KMT5C therefore

52   demonstrates that phase separation can achieve robust compartmentalization while nevertheless

53   retaining liquid-like mobility.

54   Consistent with this behavior, KMT5C was more efficient in chromocenter localization

55   than CBX5 (Fig. 1d, e). Unexpectedly, this enrichment did not simply reflect retention because

56   the unrelated MeCP2 protein had a high partition coefficient (Fig. 1d, e) but underwent

57   nucleoplasmic exchange (Fig. 1a). MeCP2 therefore defined a third state with regard to

58   partitioning and mobility, indicating these parameters were separable and occur across a

59   continuum. Intrinsically disordered regions are also typical of phase-separated proteins,[13,14]

60   including CBX5.[1,2] Although these features were highly conserved in disorder plots of CBX5

61   and MeCP2 from representative mammals, they varied for KMT5C along with charge properties

62   (Fig. 2a, Extended Data Table 1). Whereas MeCP2 had the highest overall percentage of disorder

63   (76.7), KMT5C exhibited the lowest (33.6), lacked extended regions of disorder, and its profile

64   was most divergent (Fig. 2a, Extended Data Table 1). This suggests that while CBX5 and

65   MeCP2 have prototypic features of phase separating proteins, KMT5C achieves demixing

66   through other means. To this end, CBX5 and MeCP2 contain highly conserved domains that

67   confer localization to constitutive heterochromatin (Fig. 2a),[15-17] which for KMT5C involves a

68   C-terminal region[12] that we will refer to as the Chromocenter Retention Domain (CRD).

69   Sequence identity within the CRD, however, was limited to 18 of 59 residues across mammals

3

70 (Fig. 2b) and its disorder potential and charge properties (Fig. 2c, Extended Data Table 1) varied

71 considerably (Fig. 2d). To broadly establish functional relevance of the CRD, we assessed

72 versions from *Homo sapiens* (*Hs*) and *Mus musculus* (*Mm*), together with *Cavia porcellus* (*Cp*)

73 and *Bubalus bubalis* (*Bb*) because they exhibited distinct disorder profiles and the greatest range

74 in pI (8.94-11.92) (Fig. 2c, d). Nevertheless, each CRD derivative displayed robust chromocenter

75 partitioning (Fig. 2e, f) that was not significantly different from full-length KMT5C, together

76 with intra-chromocenter mobility and limited exchange (Fig. 2g, Extended Data Videos 6-9). As

77 a result, the dynamic properties of full-length KMT5C can be entirely recapitulated by this short

78 protein segment. Although best exemplified by the mouse CRD, the behavior was shared by all

79 orthologs, suggesting it is driven by common sequence features that are modulated by species-

80 specific differences.

81 We next examined the role of conserved residues in the CRD, focusing on $C^{362}C^{366}$,

82 $H^{357}H^{365}$, and $W^{359}W^{390}W^{392}Y^{396}$ (Fig. 2b), because they resembled features found in chromatin

83 reader modules that jointly recognize DNA and histones.[18] Mutation of individual motifs caused

84 elevated exchange in FRAP assays (Fig. 3a, Extended Data Videos 10-12), which was

85 accompanied by increased nucleoplasmic abundance (Fig. 3b) and decreased partitioning (Fig.

86 3c, d). Combining mutants ($C^{366}W^{390}W^{392}$) abrogated chromocenter localization and led to rapid

87 mobility (Fig. 3a-d, Extended Data Video 13). These findings established that the CRD has

88 evolved multiple determinants that cooperate to confer localization and limit its exit from

89 individual chromocenters, while still supporting a liquid-like state. Non-membranous organelles

90 that form by phase separation are typically spherical, reflecting a reduction in their surface

91 area,[19] which prompted us to evaluate this parameter in CRD mutants (Fig. 3e). Importantly,

92 each of the mutants caused a reduction in sphericity that correlated with their partitioning and

4

93   dynamic behavior (Fig. 3a-d), with $C^{362}C^{366}$ being most severe and $W^{359}W^{390}W^{392}Y^{396}$ the least.

94   The extent mutants perturbed CRD activity therefore reflected the degree to which they reduced

95   the valency or interaction affinity, a finding that is consistent with the behavior of other phase

96   separated proteins.[13] We extended this analysis to include KMT5C, CBX5, MeCP2, and the

97   remaining CRDs. Strikingly, KMT5C supported a significantly higher degree of sphericity than

98   either CBX5 or MeCP2 (Extended Data Fig. 1a), indicating it was more effective at generating

99   surface tension at the boundary between the chromocenter and nucleoplasm. Moreover, all CRDs

100   shared this property (Extended Data Fig. 1b), further highlighting that this domain is the key

101   determinant of the biophysical characteristics of KMT5C.

102   Phase separation by CBX5 is abrogated in *Suv39h1/2* null cells or by mutation that

103   disrupts H3K9me3 recognition,[1] underscoring the importance of this interaction in seeding liquid

104   demixing. We found the dynamic behavior of KMT5C exhibited the same dependency, reflected

105   by its increased mobility and dispersal in cells lacking SUV39H1/2 (Fig. 4a, Extended Data

106   Videos 14, 15). MECP2, however, displayed more efficient localization and slightly reduced

107   mobility (Extended Data Fig. 2), indicating the chromocenter can support distinct phase

108   separated assemblies depending on chromatin context. Another facet of phase separation

109   involves its reversibility in response to cellular queues.[13] To this end, we evaluated the histone

110   deacetylase inhibitor Trichostatin A (TSA) because it was known to cause CBX5 displacement

111   from pericentromeric heterochromatin and increase its mobility.[20] KMT5C, however, largely

112   retained chromocenter localization, but with elevated nucleoplasmic exchange (Fig. 4b,

113   Extended Data Video 16), indicating hyperacetylation differentially affects KMT5C and CBX5

114   demixing in cells. Nevertheless, this modest KMT5C release was associated with a marked

115   accumulation of H4K20me3 outside of chromocenters (Fig. 4b), establishing that retention is

5

116   essential to the spatial regulation of its enzymatic activity, which otherwise acts promiscuously.

117   Alteration of KMT5C dynamics was also apparent upon induction of DNA damage within

118   chromocenters by laser microirradiation, which is known to induce heterochromatin

119   decompaction and changes in histone post-translational modifications.[21] Specifically, bisection

120   of chromocenters using laser microirradiation caused loss of KMT5C from the damaged area,

121   creating two lobes that preserved the mobility and retention behavior of the original domain (Fig.

122   4c, Extended Data Videos 17, 18). Unlike the global change observed with TSA treatment, this

123   reflected a locally confined and precise dissolution in response to underlying chromatin state

124   changes over a timescale of seconds. Again, the behavior of KMT5C was markedly different

125   than either CBX5 or MeCP2, which showed residual localization in the damage zone and rapid

126   mobility (Fig. 4c, d, and Extended Data Videos 19-22). Collectively, these findings indicate that

127   phase separation can tune constitutive heterochromatin protein content and dynamics in response

128   to changes in chromatin state and environmental stimuli.

129   The CRD provides a minimalist model to decipher how phase separation can support

130   spatial confinement while at the same time maintaining liquid-like behavior. Although lacking

131   many of the typical sequence features of phase separating proteins,[3,13] the CRD met the criterion

132   of multivalency. Nevertheless, while this normally controls the composition and biophysical

133   properties of phase separated assemblies via low affinity interactions that allow proteins to

134   exchange with their surroundings,[3] the CRD underwent very limited exchange. In this regard,

135   CRD mutants resembled full-length CBX5 in mobility and partitioning, indicating multiple

136   determinants act in a highly synergistic manner to self-reinforce chromocenter retention. This

137   behavior was independently supported by the response of KMT5C to inhibition of HDACs (Fig.

138   4), which partially diminished retention. For *Drosophila* HP1a, H3K9me3 recognition is driven

6

139 by cation-π interactions involving a triad of aromatic residues (Y^{24}, W^{45}, and Y^{48}) within the

140 chromodomain,[15] and is necessary for heterochromatin phase separation.[2] A key difference in the

141 CRD is the presence of five aromatic residues (W^{359} , W^{384}, W^{390}, W^{392}, and Y^{396}) and the

142 predominance of tryptophan, which confers the strongest cation-π interactions[22] and supports

143 more stable binding of trimethyllysine.[23] Together with multivalency and the capacity for π-π

144 interactions,[24] the CRD appears to have evolved unique determinants that are optimized to

145 confine KMT5C to constitutive heterochromatin. Moreover, when compared to other phase

146 separating proteins, this activity has been consolidated into a limited number of sequence

147 features that are sufficient to reduce chromocenter surface area and enable exquisite control of

148 protein localization in the aqueous phase.

149 Phase separation can be described in phase diagrams where changes in protein

150 concentration and interaction strength give rise to assemblies with distinct material properties,[19]

151 including gels, glassy solids, and pathological aggregates.[13] The latter are states where molecules

152 are immobile, retain their relative positions to each other, and do not exchange with their

153 surroundings.[19] This is clearly not what we have described for KMT5C, which remained in a

154 liquid state despite limited exchange that initially suggested it was immobile.[12] Although in

155 principle high partitioning to a phase separated compartment has the potential to drive retention,[3]

156 the behavior of MeCP2 indicates that this feature alone is not sufficient, but also requires a high

157 energy barrier to exit. For KMT5C, this combination allows it to be effectively biocontained

158 within a phase separated 'organelle' and affords tight spatial control of H4K20me3 catalysis.

159 This is notable given it constitutes a minority of the methylated H4K20 pool[25] and is primarily

160 associated with satellite and other distinct repeats.[26] This control is lost when KMT5C is no

161 longer constrained in demixed assemblies (Fig. 4). Moreover, the opposing behaviors of KMT5C

7

162   and MeCP2 indicated that change of a single epigenetic feature can dramatically reprogram the

163   phase separated state with regard to protein composition and dynamics. Of particular relevance

164   to this finding, MeCP2 loss in a mouse model of Rett syndrome leads to H4K20me3 gain in the

165   chromocenter, supporting an antagonistic relationship with KMT5C *in vivo* at endogenous

166   protein levels.[27] This principle is also supported by an altered chromocenter proteome in

167   *Suv39h1/2* knockout cells[28] and the established plasticity of constitutive heterochromatin in

168   development and disease.[29] The existence of these distinct phase separated states therefore

169   provides a conceptual framework to understand the drivers of normal and pathogenic

170   chromocenter homeostasis. By considering chromatin as a multivalent scaffold, we can decipher

171   how changes in epigenetic features and the mutational status of resident proteins shift the

172   composition and function of phase separated assemblies.

8

173 **Methods**

174 **Cell Culture and transfection**

175 Cells were cultured at 37°C and 5% CO_2 in a humidified incubator. All cell lines were grown in

176 DMEM containing 10% FBS. D5 (*Suv39h1/2* knockout) and W8 (*Suv39h1/2* wild-type) mouse

177 embryonic fibroblast cells lines[8] were obtained from Dr. Thomas Jenuwein. All other analyses

178 were carried out using the mouse NMuMG breast cell line. Cells were transfected by lipofection

179 using Effectene (Qiagen) 1 day prior to experiments. Expression plasmids were synthesized

180 (www.biomatik.com), obtained from the Addgene repository (www.addgene.org), or previously

181 described[30] (sequences provided in supplemental material).

182

183 **Live-cell imaging**

184 Live cell imaging was carried out using Zeiss Axiovert 200M inverted microscopes attached to

185 either an LSM510 NLO laser scanning system with a 25 mW argon laser line, a Zeiss LSM 770

186 confocal microscope attached to an Axio Observer Z3 equipped with 405, 488, 561, and 633 nm

187 diode lasers, or a PerkinElmer Ultraview spinning-disk confocal microscope equipped with 405,

188 488, and 561 nm diode lasers and a FRAP-unit. For all platforms, a 40 x 1.3 NA oil immersion

189 lens was used. Long-term live-cell observations were conducted on the spinning disk microscope

190 at 37°C in a humidified atmosphere containing 5% CO_2. In cases were Z-stacks were acquired,

191 spacing was set at 400 nm. Fluorescence recovery after photobleaching was performed on

192 transiently transfected cells using the 488 nm solid state (spinning disk confocal) or 488 nm

193 argon laser line (LSM 510). Circular (chromocenter) or linear (nucleoplasm) regions were

194 demarcated and subsequently bleached by intense light from the 488 nm laser. Fluorescence

195 recovery of the bleached regions was quantified over multiple time scales (seconds to minutes).

9

196   FRAP data was extracted using Zeiss LSM 5 Zen or ImageJ software by measuring fluorescence

197   intensity of the background, the whole nucleus and the bleached area in each of the recorded

198   time-lapse pictures for a minimum of 30 cells. Normalized relative intensity (including standard

199   deviation) was calculated in Microsoft Excel and plotted using Graphpad Prism software. Laser

200   microirradiation experiments were performed using the spinning disk microscope using the 100 x

201   1.4 NA objective lens. Cells were grown in MatTek 35 mm glass bottom dishes and were

202   sensitized with 1 µg/µl Hoechst 20 min prior to the experiment. After calibration of the

203   photokinesis device, a thin horizontal line representing the region to be microirradiated was

204   placed so that it divided the chromocenter into approximately two equal parts. Laser

205   microirradiation was carried out by using 20% power of the 405 nm solid state laser and 10

206   iterations. Images were acquired at defined time intervals using laser and filter settings for GFP

207   imaging. Subsequent photobleaching of the non-microirradiated portion of chromocenters was

208   done using 10 iterations at 100% power of the 488 nm solid state laser.

209

210   **Immunofluorescence**

211   Cells grown on adherent coverslips were fixed in 4% paraformaldehyde in PBS for 10 min,

212   permeabilized in 0.5 % Triton X-100 in PBS for 5min and then incubated with primary

213   antibodies diluted in PBS. After 30 min at room temperature, the cells were washed once with

214   0.1 % Triton X-100 in PBS for 1 min then rinsed 3 times with PBS prior to addition of secondary

215   antibodies diluted in PBS. Cells were incubated for 30 min at room temperature, washed with 0.1

216   % Triton X-100 in PBS for 1 min and rinsed three times with PBS. Coverslips were mounted

217   onto microscope slides with in-house made polyvinyl alcohol mounting media containing 1

218   µg/mL 4′,6-diamidino-2-phenylindole (DAPI). Z-Stacks were obtained on a Zeiss Imager.Z1

10

219   equipped with a Photometrics Prime BSI camera and Metamorph software version 7.10.2.240

220   (Molecular Devices, Sunnyvale, CA) using a Zeiss 63 x 1.3 NA oil lens. Step size used was 0.2

221   μm. Primary antibodies and dilutions were as follows: α-H4K20me3 (Active Motif 39672),

222   1:500; and α-H3K9me3 (Active Motif 3916). Secondary antibodies and dilutions were as

223   follows: goat α-mouse Alexa-488, 1:500; goat α-rabbit Alexa-488 1:500; and goat α-mouse

224   Cy3, 1:500.

225

226   **Image analysis**

227   Images were deconvolved with Huygens Professional version 19.04 (Scientific Volume Imaging,

228   http://svi.nl). Z-stacks were imported into Imaris 9.3 (Oxford Instruments) and cropped to

229   generate 3D images of single nuclei. The Imaris *surfaces* function was used to encapsulate all

230   chromocentres with a shell and the *statistics* function was used to measure the volume,

231   sphericity, and total number of chromocenters for output to a Microsoft Excel spreadsheet.

232   Graphical representation of the data was prepared using the PlotsOfDifferences server

233   (https://huygens.science.uva.nl/PlotsOfDifferences/).[31] For partition coefficients, line scans

234   through nuclei of undeconvolved 3D images were recorded using ImageJ. For each cell, the

235   partition coefficient was calculated by subtracting the background level from the maxima of the

236   brightest chromocenter and dividing it by the background corrected fluorescence intensity of the

237   nucleoplasm. For each protein analyzed, measurements were taken from n>10 nuclei.

238

239   **Statistical analysis**

240   For partition coefficients, significance was evaluated using the Kruskal-Wallis one-way analysis

241   test and individual comparisons between proteins were done using the Wilcoxon rank sum test.

11

242   Statistical significance of sphericity data was evaluated using the embedded stats function within

243   PlotsOfDifferences, which calculates p-values using a randomization test.[31]

12

References

244

245   1   Larson, A. G. *et al.* Liquid droplet formation by HP1alpha suggests a role for phase

246   separation in heterochromatin. *Nature* **547**, 236-240, doi:10.1038/nature22822 (2017).

247   2   Strom, A. R. *et al.* Phase separation drives heterochromatin domain formation. *Nature*

248   **547**, 241-245, doi:10.1038/nature22989 (2017).

249   3   Banani, S. F., Lee, H. O., Hyman, A. A. & Rosen, M. K. Biomolecular condensates:

250   organizers of cellular biochemistry. *Nat Rev Mol Cell Biol* **18**, 285-298,

251   doi:10.1038/nrm.2017.7 (2017).

252   4   Alberti, S. The wisdom of crowds: regulating cell function through condensed states of

253   living matter. *J Cell Sci* **130**, 2789-2796, doi:10.1242/jcs.200295 (2017).

254   5   Haaf, T. & Schmid, M. Chromosome topology in mammalian interphase nuclei. *Exp Cell*

255   *Res* **192**, 325-332 (1991).

256   6   Erdel, F. & Rippe, K. Formation of Chromatin Subcompartments by Phase Separation.

257   *Biophysical journal* **114**, 2262-2270, doi:10.1016/j.bpj.2018.03.011 (2018).

258   7   Larson, A. G. & Narlikar, G. J. The Role of Phase Separation in Heterochromatin

259   Formation, Function, and Regulation. *Biochemistry* **57**, 2540-2548,

260   doi:10.1021/acs.biochem.8b00401 (2018).

261   8   Peters, A. H. *et al.* Loss of the Suv39h histone methyltransferases impairs mammalian

262   heterochromatin and genome stability. *Cell* **107**, 323-337 (2001).

263   9   Cheutin, T. *et al.* Maintenance of stable heterochromatin domains by dynamic HP1

264   binding. *Science* **299**, 721-725, doi:10.1126/science.1078572 (2003).

13

265   10   Muller-Ott, K. *et al.* Specificity, propagation, and memory of pericentric

266   heterochromatin. *Molecular systems biology* **10**, 746, doi:10.15252/msb.20145377

267   (2014).

268   11   Kumar, A. *et al.* Analysis of protein domains and Rett syndrome mutations indicate that

269   multiple regions influence chromatin-binding dynamics of the chromatin-associated

270   protein MECP2 in vivo. *J Cell Sci* **121**, 1128-1137, doi:10.1242/jcs.016865 (2008).

271   12   Hahn, M. *et al.* Suv4-20h2 mediates chromatin compaction and is important for cohesin

272   recruitment to heterochromatin. *Genes Dev* **27**, 859-872, doi:10.1101/gad.210377.112

273   (2013).

274   13   Shin, Y. & Brangwynne, C. P. Liquid phase condensation in cell physiology and disease.

275   *Science* **357**, doi:10.1126/science.aaf4382 (2017).

276   14   Zhu, L. & Brangwynne, C. P. Nuclear bodies: the emerging biophysics of nucleoplasmic

277   phases. *Curr Opin Cell Biol* **34**, 23-30, doi:10.1016/j.ceb.2015.04.003 (2015).

278   15   Jacobs, S. A. & Khorasanizadeh, S. Structure of HP1 chromodomain bound to a lysine 9-

279   methylated histone H3 tail. *Science* **295**, 2080-2083, doi:10.1126/science.1069473

280   (2002).

281   16   Nielsen, P. R. *et al.* Structure of the HP1 chromodomain bound to histone H3 methylated

282   at lysine 9. *Nature* **416**, 103-107, doi:10.1038/nature722 (2002).

283   17   Ohki, I. *et al.* Solution structure of the methyl-CpG binding domain of human MBD1 in

284   complex with methylated DNA. *Cell* **105**, 487-497 (2001).

285   18   Weaver, T. M., Morrison, E. A. & Musselman, C. A. Reading More than Histones: The

286   Prevalence of Nucleic Acid Binding among Reader Domains. *Molecules* **23**,

287   doi:10.3390/molecules23102614 (2018).

14

288   19   Hyman, A. A., Weber, C. A. & Julicher, F. Liquid-liquid phase separation in biology.

289   *Annu Rev Cell Dev Biol* **30**, 39-58, doi:10.1146/annurev-cellbio-100913-013325 (2014).

290   20   Taddei, A., Maison, C., Roche, D. & Almouzni, G. Reversible disruption of pericentric

291   heterochromatin and centromere function by inhibiting deacetylases. *Nat Cell Biol* **3**,

292   114-120, doi:10.1038/35055010 (2001).

293   21   Murray, J. M., Stiff, T. & Jeggo, P. A. DNA double-strand break repair within

294   heterochromatic regions. *Biochemical Society transactions* **40**, 173-178,

295   doi:10.1042/BST20110631 (2012).

296   22   Dougherty, D. A. Cation-pi interactions in chemistry and biology: a new view of

297   benzene, Phe, Tyr, and Trp. *Science* **271**, 163-168, doi:10.1126/science.271.5246.163

298   (1996).

299   23   Riemen, A. J. & Waters, M. L. Design of highly stabilized beta-hairpin peptides through

300   cation-pi interactions of lysine and n-methyllysine with an aromatic pocket. *Biochemistry*

301   **48**, 1525-1531, doi:10.1021/bi801706k (2009).

302   24   Vernon, R. M. *et al.* Pi-Pi contacts are an overlooked protein feature relevant to phase

303   separation. *eLife* **7**, doi:10.7554/eLife.31486 (2018).

304   25   Pesavento, J. J., Yang, H., Kelleher, N. L. & Mizzen, C. A. Certain and progressive

305   methylation of histone H4 at lysine 20 during the cell cycle. *Mol Cell Biol* **28**, 468-486

306   (2008).

307   26   Mikkelsen, T. S. *et al.* Genome-wide maps of chromatin state in pluripotent and lineage-

308   committed cells. *Nature* **448**, 553-560 (2007).

15

309 27 Linhoff, M. W., Garg, S. K. & Mandel, G. A high-resolution imaging approach to

310   investigate chromatin architecture in complex tissues. *Cell* **163**, 246-255,

311   doi:10.1016/j.cell.2015.09.002 (2015).

312 28 Saksouk, N. *et al.* Redundant mechanisms to form silent chromatin at pericentromeric

313   regions rely on BEND3 and DNA methylation. *Mol Cell* **56**, 580-594,

314   doi:10.1016/j.molcel.2014.10.001 (2014).

315 29 Dejardin, J. Switching between Epigenetic States at Pericentromeric Heterochromatin.

316   *Trends Genet* **31**, 661-672, doi:10.1016/j.tig.2015.09.003 (2015).

317 30 Tsang, L. W., Hu, N. & Underhill, D. A. Comparative analyses of SUV420H1 isoforms

318   and SUV420H2 reveal differences in their cellular localization and effects on myogenic

319   differentiation. *PLoS ONE* **5**, e14447, doi:10.1371/journal.pone.0014447 (2010).

320 31 Goedhart, J. PlotsOfDifferences – a web app for the quantitative comparison of unpaired

321   data. *bioRxiv*, 578575, doi:10.1101/578575 (2019).

322 32 Sievers, F. *et al.* Fast, scalable generation of high-quality protein multiple sequence

323   alignments using Clustal Omega. *Molecular systems biology* **7**, 539,

324   doi:10.1038/msb.2011.75 (2011).

325 33 Peng, K. *et al.* Optimizing long intrinsic disorder predictors with protein evolutionary

326   information. *J Bioinform Comput Biol* **3**, 35-60 (2005).

327 34 Drozdetskiy, A., Cole, C., Procter, J. & Barton, G. J. JPred4: a protein secondary

328   structure prediction server. *Nucleic Acids Res* **43**, W389-394, doi:10.1093/nar/gkv332

329   (2015).

330 35 Schotta, G. *et al.* A silencing pathway to induce H3-K9 and H4-K20 trimethylation at

331   constitutive heterochromatin. *Genes Dev* **18**, 1251-1262 (2004).

332

16

333 **Extended Data**

334 **Videos**

335 Video 1; KMT5C FRAP

336 Video 2; MeCP2 FRAP

337 Video 3; CBX5 FRAP

338 Video 4; Partial KMT5C bleach (doughnut)

339 Video 5; Partial KMT5C bleach (bridge)

340 Video 6; *Homo sapiens* CRD FRAP

341 Video 7; *Mus musculus* CRD FRAP

342 Video 8; *Cavia porcellus* CRD FRAP

343 Video 9; *Bubalus bubalis* CRD FRAP

344 Video 10; $CRDC^{362}C^{366}$ FRAP

345 Video 11; $CRDH^{357}H^{365}$ FRAP

346 Video 12; $CRDW^{359}W^{390}W^{392}Y^{396}$ FRAP

347 Video 13; $CRDC^{366}W^{390}W^{392}$ FRAP

348 Video 14; KMT5C in D5; *Suv39h1/2* knockout FRAP

349 Video 15; KMT5C in W8; *Suv39h1/2* wild-type FRAP

350 Video 16; KMT5C with TSA FRAP (no TSA control; Video 1)

351 Video 17; KMT5C laser microirradiation

352 Video 18, KMT5C laser microirradiation + FRAP

353 Video 19; MeCP2 laser microirradiation

354 Video 20, MeCP2 laser microirradiation + FRAP

355 Video 21; CBX5 laser microirradiation

17

356   Video 22, CBX5 laser microirradiation + FRAP

357

358   **Figures and Tables**

359   Table 1; Spreadsheet 1; PCH PONDR excel; additional species disorder and physicochemical

360   data for KMT5C, MeCP2, CBX5, and CRD

361   Figure 1; Sphericity data for (a) KMT5C, MeCP2, CBX5, (b) *Hs*, *Cp*, *Bb*, and *Cp* CRDs, and (c)

362   wild-type and mutant CRDs.

363   Figure 2; MeCP2 (a) localization and (b) mobility in D5 (*Suv39h1/2* knockout) and W8

364   (*Suv39h1/2* wild-type) cells

18

365 **Acknowledgements**

371

372 **Author Contributions**

373 D.A.U. and M.J.H. conceived the project. D.A.U., M.J.H, and H.S. designed all experiments and

374 interpreted data. K.M. made the initial observation of KMT5C mobility and performed FRAP

375 and fluorescence imaging experiments. H.S. performed live-cell imaging, laser micro-irradiation,

376 and partition coefficient analyses. D.A.U. carried out sequence analysis and expression plasmid

377 design. D.A.U. wrote the manuscript with contributions from M.J.H. and H.S. D.A.U. prepared

378 figures with contributions from H.S. and K.M.

379

380 **Containing data deposition statement**

381 N/A

382

383 **Competing interests**

384 The authors declare no competing interests.

385

19

386   **Corresponding author line**

387   D. A. Underhill Department of Oncology, 2328 Cross Cancer Institute, 11560 University

388   Avenue, Edmonton, Alberta, Canada, T6G 1Z2. Phone: (780) 432-8903, Fax: (780) 432-8892,

389   E-mail: **alan.underhill@ualberta.ca**

20

390 **Figure 1. KMT5C is mobile within chromocenters but undergoes limited nucleoplasmic**

391 **exchange**. **a,** FRAP curves for KMT5C, MeCP2, and CBX5-mEmerald fusion proteins in mouse

392 NMuMG breast cancer cells (*n=30*) (see Methods). Partial (*red*) and full (*blue*) fluorescence

393 recovery curves (*filled circles* represent mean fluorescence intensity, while *vertical lines* indicate

394 standard deviation. **b,** Time-lapse series of *full* and *partial* KMT5C-mEmerald photobleaching

395 (Extended Data Movie 4). Insets use a 16-color intensity map to depict fluorescence recovery

396 upon partial or full bleaching from 0.3 to 60s.The second *partial* panel depicts an independent

397 recovery event involving a chromatin bridge between two chromocenters (Extended Data Movie

398 5), indicating they form a contiguous phase separated environment. **c**, Schematic representation

399 of KMT5C (*green*) movement (*arrows*) in each of the full and partial bleach (*translucent circles*)

400 time series from panel **b**. **d,** Partition images (16-color intensity map) for KMT5C, CBX5 and

401 MePC2. **e,** Scatter plots display corresponding partition coefficients for KMT5B (*n=26*), MeCP2

402 (*n=30*), and CBX5 (*n=30*) (see Methods).

403

21
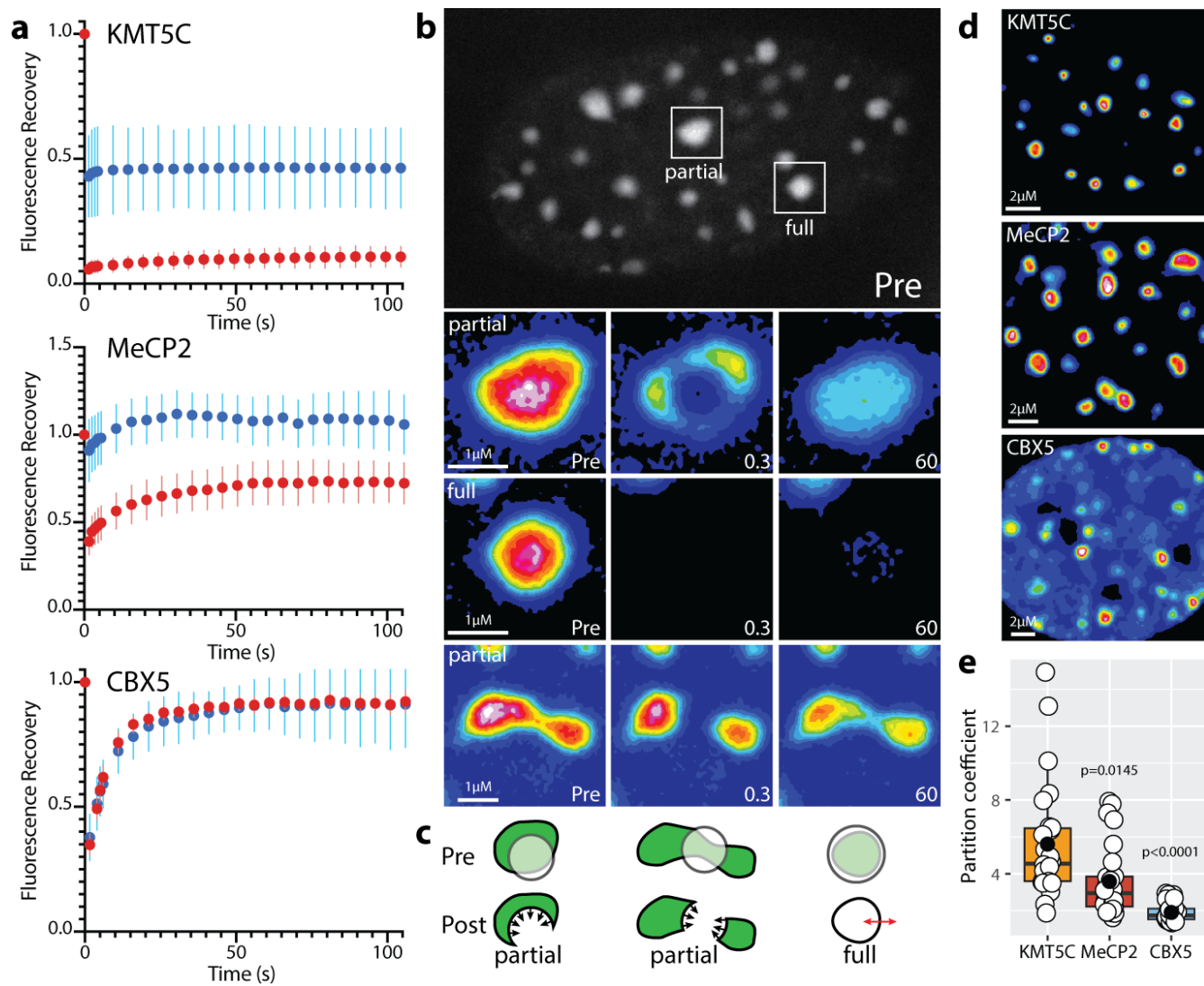
405 **Figure 2. The chromocenter retention domain constrains KMT5C to individual**

406 **chromocenters**. **a,** Disorder plots (PONDR) and charge heatmaps for KMT5C, CBX5, and

407 MeCP2 orthologs from *Homo Sapiens* (*Hs*), *Mus musculus* (*Mm*), *Bubalus bubalis* (*Bb*), and

408 *Cavia porcellus* (*Cp*). For reference, schematics illustrate the distribution of annotated domains

409 in each protein (**S**u(var)3-9, **E**nhancer-of-zeste and **T**rithorax (SET); **R**NA-**B**inding **D**omain

410 (RBD); **C**hromocenter **R**etention **D**omain; **M**ethyl-CpG **B**inding **D**omain (MBD);

411 **C**hromo**d**omain (CD); **H**inge domain (H); and **C**hromoshadow **D**omain (CD)). Input sequences

412 were aligned using Clustal Omega[32] together with manual removal of gaps and then analyzed for

413 disorder using PONDR[33] and charge properties using EMBOSS. Average disorder percentage

414 and score are indicated to the *right* of the primary structure schematic, and disordered segments

415 are shown as thick horizontal lines. **b,** Multispecies sequence alignment of the CRD is shown in

416 JPred[34] format. Residues absolutely conserved in mammals are indicated by a *filled circle*, while

417 those exhibiting 90% conservation are noted by *open circles*. Amino acids selected for

418 mutagenesis are numbered. **c,** Disorder plots and charge heatmaps are shown for the CRD

419 (species and details are as described in panel *a*). **d,** Scatter plots of isoelectric point, disorder

420 score, disorder %, and disorder length for CBX5, CRD, KMT5C, and MeCP2 across 20

421 representative mammalian species (Extended Data Table 1). **e,** Partition images (16-color

422 intensity map) for the CRD from *Hs*, *Mm*, *Cp*, and *Bb* indicate that all effectively partition to

423 chromocenters. **f,** Partition coefficient graph for *Hs* (*n=39*), *Mm* (*n=30*), *Cp* (*n=23*), and *Bb*

424 (*n=26*) CRDs demonstrate high chromocenter partitioning. Full-length KMT5C is shown for

425 reference (*faded*). **g,** FRAP analyses of *Hs*, *Mm*, *Cp*, and *Bb* CRD domains (Extended Data

426 Movies 6-9) support intra-chromocenter mobility with reduced nucleoplasmic exchange (*n=30*).

427

23

428
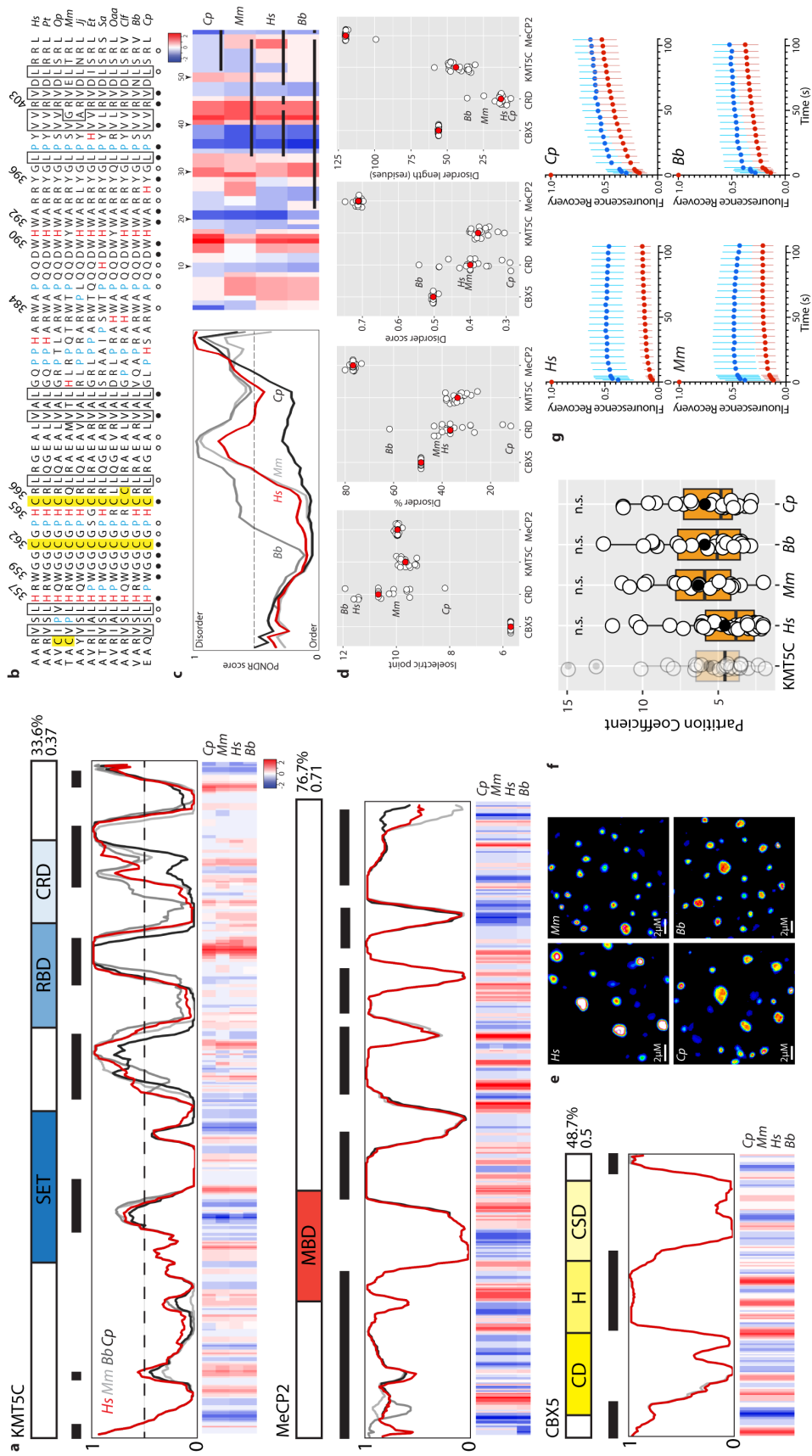
429   **Figure 3. The CRD comprises multiple determinants that cooperate to drive**

430   **heterochromatin phase separation. a,** FRAP analysis of CRD mutants that target conserved

431   sequence features ($C^{362}C^{366}$, $H^{357}H^{365}$, and $W^{359}W^{390}W^{392}Y^{396}$) or combinations thereof

432   ($C^{366}W^{390}W^{392}$) (*n=30*). Wild-type KMT5C (*faded*) is shown in the upper left panel for reference

433   (Extended Data movies 10-13). While the recovery profiles are similar for the $C^{362}C^{366}$ and

434     $H^{357}H^{365}$ mutants, they differed for the $W^{359}W^{390}W^{392}Y^{396}$ and mutants, suggesting they affect

435   distinct interactions. **b,** Partition images (16-color intensity map) for CRD mutants. **c,** Partition

436   coefficients for CRD mutants (WT (*n=39*), Trp (*n=18*), His (*n=17*), and Cys (*n=20*)). **d,**

437   Schematic summary illustrates that mutants continue to localize to the chromocenter, but now

438   readily exchange with the cytoplasmic pool. **e,** Sphericity analysis of the wild-type (*n=990*) and

439   mutant (Trp (*n=437*), His (*n=1834*), and Cys (*n=1054*) CRDs (see Methods).

440

25
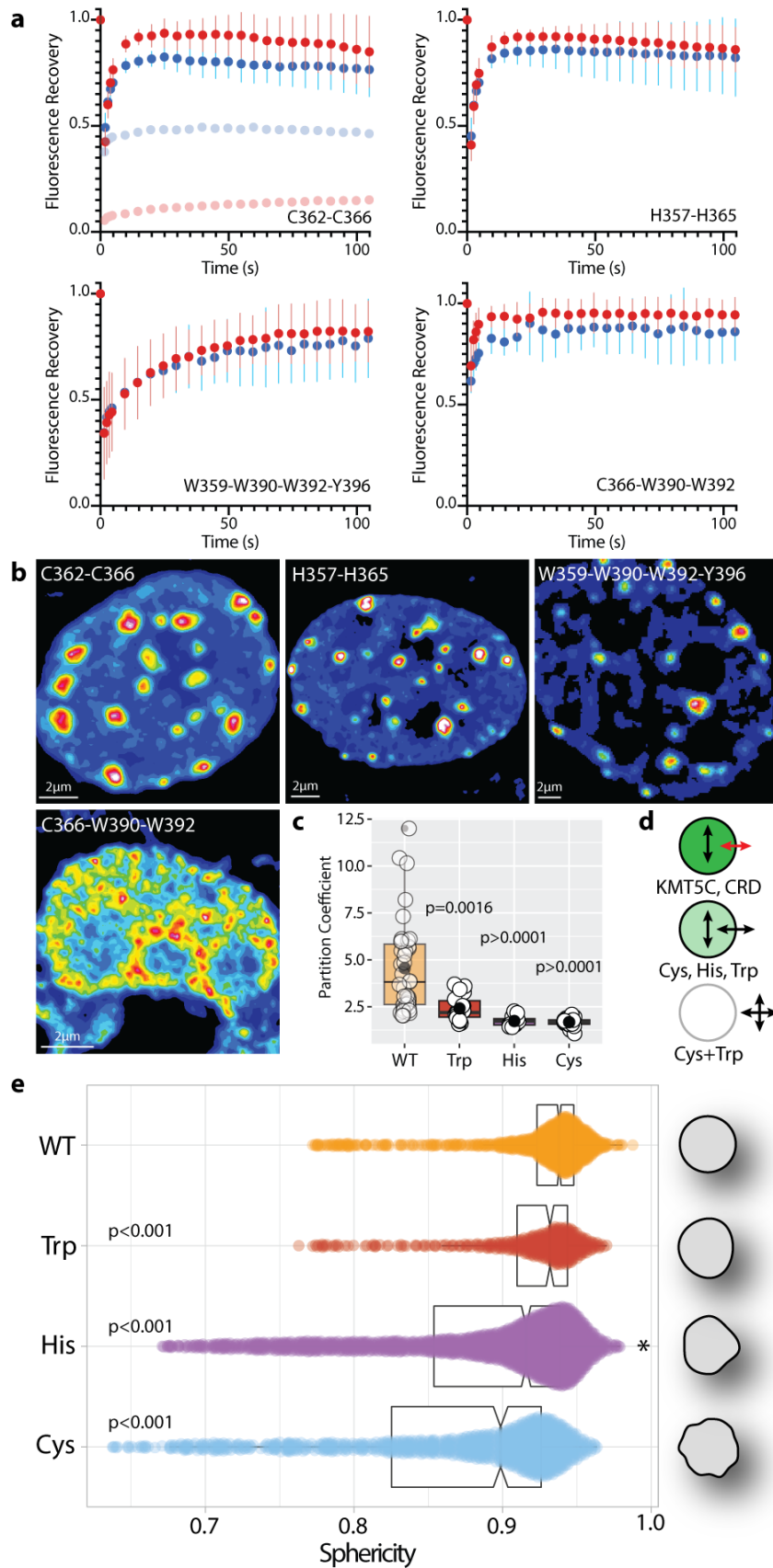
443   **Figure 4. KMT5C phase separation is rapidly reversible and responsive to underlying**

444   **chromatin state**. **a,** KMT5C localization and mobility in *Suv39h1/2* knockout cells. *Top row*,

445   KMT5C localization is dependent on H3K9me3 placement by SUV39H1/2[35] which leads to

446   redistribution of H4K20me3 (*middle row*) and marked in increase in KMT5C mobility in

447   *Suv39h1/2* knockout cells when assessed by FRAP (*bottom row* and Extended Data Videos 14,

448   15) (*n=30*). **b,** The histone deacetylase inhibitor trichostatin A (TSA) alters KMT5C localization

449   and mobility, and leads to H4K20me3 redistribution (treatment was for 16-24hrs at 100nM).

450   *Upper row,* KMT5C localization is only moderately affected by TSA treatment, but H4K20me3

451   undergoes dramatic redistribution (*middle row*) that coincides with increased KMT5C

452   nucleoplasmic exchange in FRAP (*bottom row* and Extended Data Video 16) (*n=30*). In *a* and *b*,

453   the schematic indicates H4K20me3 is no longer confined to the chromocenter under either

454   condition, but that *Suv39h1/2* knockout had a larger effect on KMT5C localization, despite

455   similar increases in mobility with TSA treatment. **c,** Laser micro-irradiation of KMT5C, MeCP2,

456   and CBX5 differentially modulates their phase separation (Extended Data Videos 17-22). For

457   each protein, the *top row* represents a time series that includes pre-damage (Pre), immediately

458   following damage (4s), and at 60s (area targeted by micro-IR is indicated by facing *arrows*). The

459   *bottom row* depicts a FRAP time series where a portion of the damaged chromocenter (*arrows* in

460   Pre-bleach) is photobleached (*red arrow*) and recovery is monitored at 4s and either 60s

461   (KMT5C) or 20s (MeCP2 and CBX5). Maximum image projections (MIP) are included to

462   highlight the area of decondensed heterochromatin following damage induction and the location

463   of the bleaching zone for mEmerald fusions of KMT5C, MeCP2, and CBX5. **d,** Comparison of

464   pre and post irradiation images for KMT5C, MeCP2 and CBX5.While MeCP2 and CBX5

465   behaved similarly and underwent only transient or no decrease in intensity over the damaged

27

466   area, KMT5C rapidly exited and accumulated in the two non-damaged lobes. **e,** Schematic

467   summary of laser microirradiation and FRAP analyses. The *left* panel summarizes the

468   experimental strategy, which involves using a laser to induce chromocenter DNA damage and

469   then characterize the behavior of the exogenously expressed fusion protein, as well as its

470   capacity to recover fluorescence following photobleaching. The DAPI series was used to monitor

471   heterochromatin decompaction following damage, while the response of the mEmerald fusion

472   protein was visualized over time at which point the lower portion of chromocenter was bleached

473   in order to determine protein mobility. In both contexts, KMT5C behaved markedly different

474   than MeCP2 and CBX5. It neither persisted in the damaged area nor exhibited fluorescence

475   recovery.

476

28

477

29
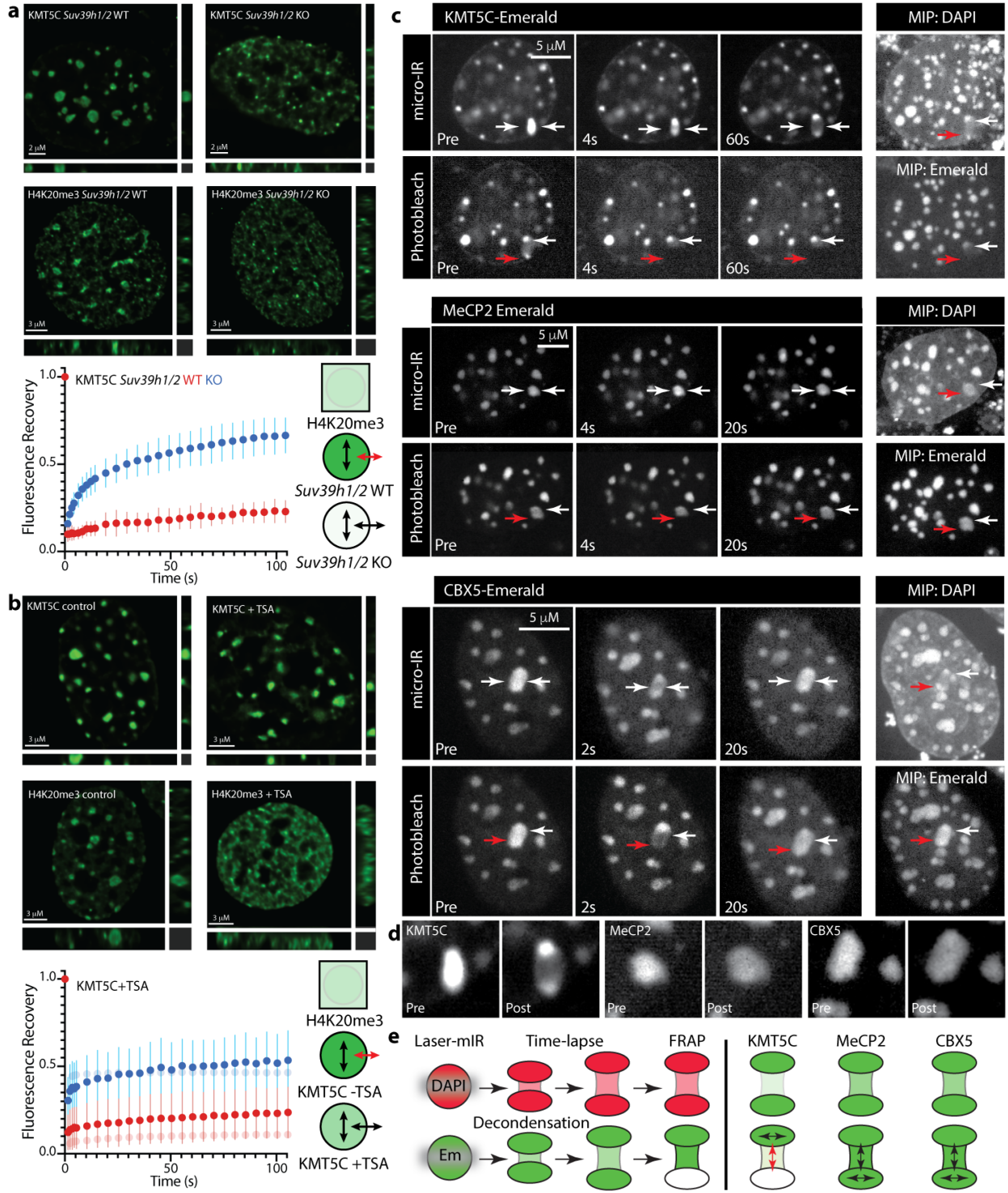
478   **Extended Data Figures and Legends**

479   **Figure 1. Chromocenter sphericity analysis of KMT5,** MeCP2**, CBX5, and all CRD**

480   **derivatives. a,** Comparison of chromocenter sphericity of full-length KMT5C (*n=775*), MeCP2

481   (*n=641*), and CBX5 (*n=644*) indicates KMT5C supports significantly higher sphericity. **b,**

482   Comparison of chromocenter sphericity generated by CRDs from *Homo sapiens* (*Hs*; *n=990*),

483   *Mus musculus* (*Mm*; *n=421*), *Bubalus bubalis* (*Bb*; *n=574*), and *Cavia porcellus* (*Cp*; *n=982*).

484   All CRDs support efficient sphericity, although this is significantly higher for *Mm*, *Bb*, and *Cp*

485   when compared to *Hs*, which also exhibited reduced chromocenter portioning (*n.s.*) (manuscript
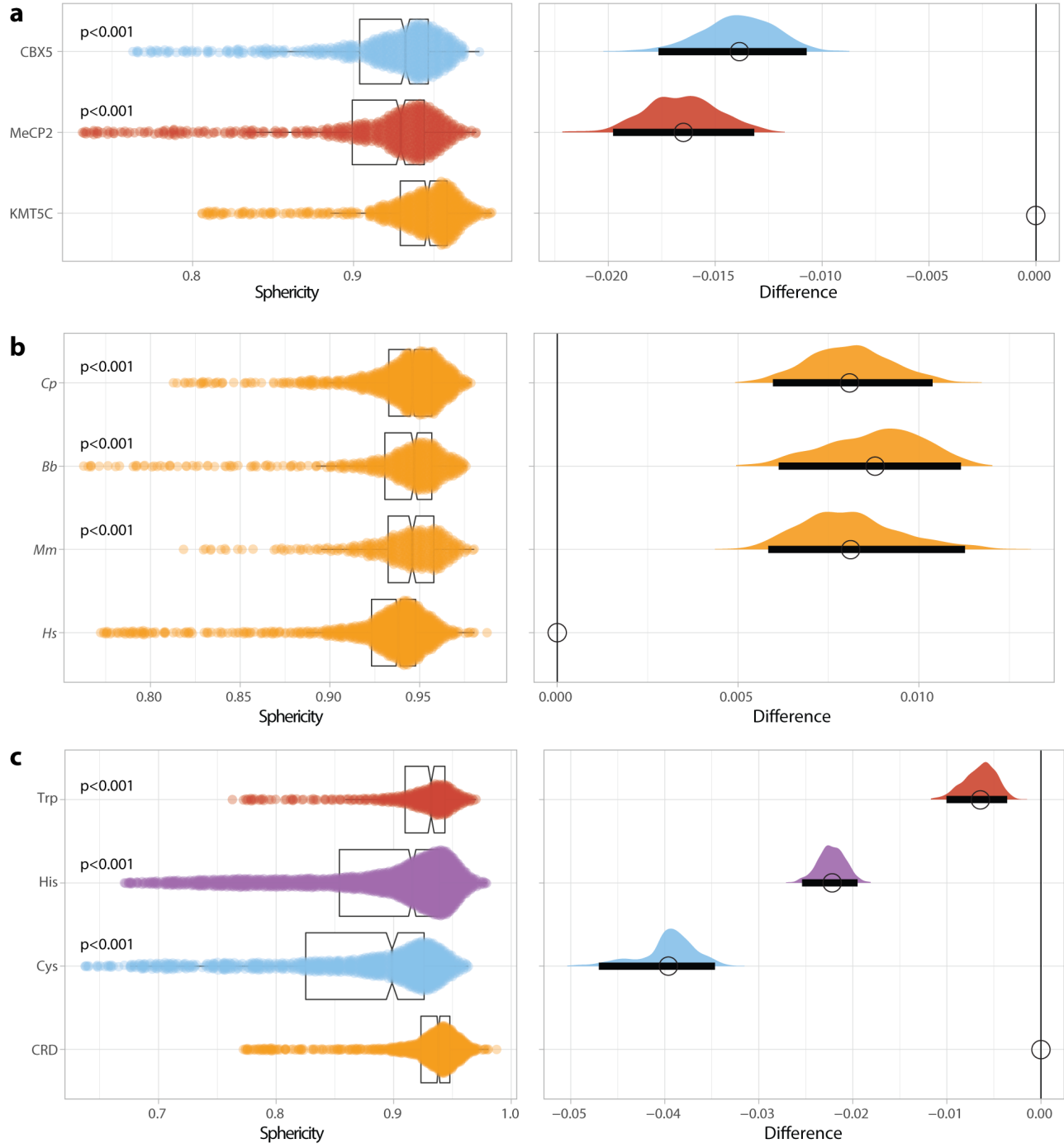
486   Fig. 2f) 2. Nevertheless, the human CRD supports significantly higher sphericity than MeCP2

487   (p<0.001) and CBX5 (p<0.001), or CRD mutants (*panel c*). **c,** Comparison of sphericity for wild-

488   type (*Hs*) and mutant CRDs (as in manuscript Fig.3e, with inclusion of difference plot). All
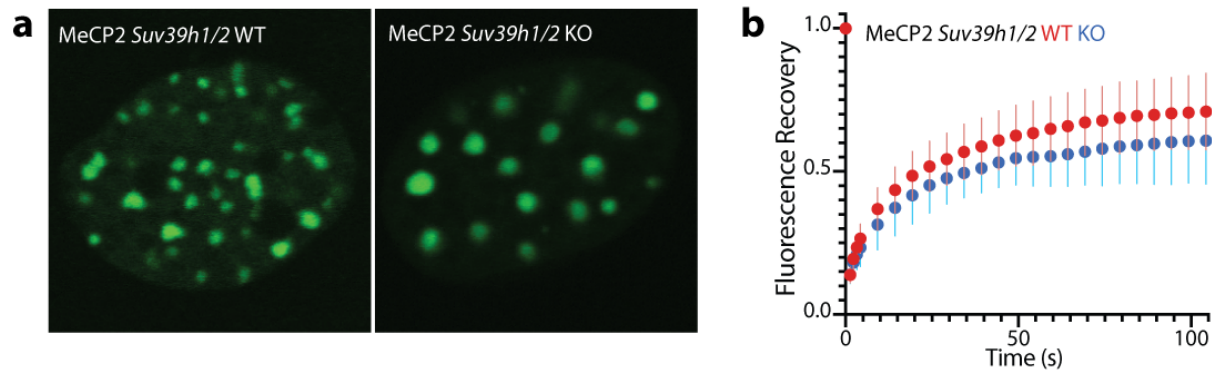
489   proteins were assessed in murine NMuMG breast cancer cells (see Methods).

490

30

491

31

492   **Figure 2. Localization and FRAP of MeCP2 in *Suv39h1/2* wild-type and knockout cells. a,**

493   MeCP2-GFP displays efficient chromocenter localization in both *Suv39h1/2* wild-type and

494   knockout mouse embryonic fibroblasts. **b,** FRAP analysis of MeCP2-GFP reveals a decrease in

495   mobility in *Suv39h1/2* knockout cells.

496

32

497

33